

EVIDENT | **OLYMPUS**

THESE ARE NOT FIREWORKS



This is a single colony of Gloeotrichia captured using a 10X X Line objective.

IMAGE: © HAKAN KVARNSTROM



See the truth with
X Line™ objectives.

Scan the code
to discover more.



Contact your local sales representative or visit
olympus-lifescience.com/this-is-xline to learn more.



Quantitative analysis of backscattered-electron contrast in scanning electron microscopy

Martin Čalkovský^{1,2}  | Erich Müller² | Dagmar Gerthsen^{1,2}

¹3DMM2O, Cluster of Excellence (EXC-2082/1–390761711), Karlsruhe Institute of Technology (KIT), Karlsruhe, Germany

²Laboratory for Electron Microscopy, Karlsruhe Institute of Technology (KIT), Karlsruhe, Germany

Correspondence

Martin Čalkovský, Engesserstr. 7 Geb. 30.22 2. OG, Zimmer 228 76131 Karlsruhe Germany. Email: martin.calkovsky@kit.edu

Abstract

Backscattered-electron scanning electron microscopy (BSE-SEM) imaging is a valuable technique for materials characterisation because it provides information about the homogeneity of the material in the analysed specimen and is therefore an important technique in modern electron microscopy. However, the information contained in BSE-SEM images is up to now rarely quantitatively evaluated. The main challenge of quantitative BSE-SEM imaging is to relate the measured BSE intensity to the backscattering coefficient η and the (average) atomic number Z to derive chemical information from the BSE-SEM image. We propose a quantitative BSE-SEM method, which is based on the comparison of Monte–Carlo (MC) simulated and measured BSE intensities acquired from wedge-shaped electron-transparent specimens with known thickness profile. The new method also includes measures to improve and validate the agreement of the MC simulations with experimental data. Two different challenging samples (ZnS/Zn(O_xS_{1-x})/ZnO/Si-multilayer and PTB7/PC₇₁BM-multilayer systems) are quantitatively analysed, which demonstrates the validity of the proposed method and emphasises the importance of realistic MC simulations for quantitative BSE-SEM analysis. Moreover, MC simulations can be used to optimise the imaging parameters (electron energy, detection-angle range) in advance to avoid tedious experimental trial and error optimisation. Under optimised imaging conditions pre-determined by MC simulations, the BSE-SEM technique is capable of distinguishing materials with small composition differences.

KEYWORDS

backscattered-electron imaging, material contrast, Monte–Carlo simulations, quantitative analysis, scanning electron microscopy

1 | INTRODUCTION

Backscattered-electron imaging is a valuable technique in scanning electron microscopy (BSE-SEM) that is used for

materials characterisation because it provides important information on the mean atomic number of the analysed specimen. The measured BSE intensity is determined by the backscattered-electron coefficient η , which describes

This is an open access article under the terms of the [Creative Commons Attribution-NonCommercial](https://creativecommons.org/licenses/by-nc/4.0/) License, which permits use, distribution and reproduction in any medium, provided the original work is properly cited and is not used for commercial purposes.

© 2022 The Authors. *Journal of Microscopy* published by John Wiley & Sons Ltd on behalf of Royal Microscopical Society.

the number of BSEs per primary electron. There are several approaches to describe η as a function of the primary electron energy, atomic number of the material, and sample tilt.^{1,2} Traditionally, BSE-SEM images provide only qualitative information on the chemical composition of the sample or the distribution of different phases. More recently, the interest in extracting quantitative information from the BSE-SEM images has significantly increased, as quantification can provide information on the chemical composition of the sample directly from a BSE-SEM image if some pre-knowledge on the material system is available. As usual, the quantification requires the comparison of experimental and simulated image intensities. Monte-Carlo (MC) simulations are well suited for the calculation of the BSE intensities and can be, hence, utilised to extract quantitative information from BSE-SEM images.^{3,4} However, the derivation of quantitative composition information is not straightforward because the measured BSE intensity is determined not only by the materials parameters but also by a complex interplay of several factors, such as imaging parameters, detection-system settings, and sample thickness, which all need to be known.

Quantitative BSE-SEM analysis has already been successfully used to identify strategic metals in minerals,⁵ to quantify concentrations of Au, Ag, Ge, Cu and Fe films on a Si substrate,⁶ and to evaluate the mineral distribution in bones.⁷ Furthermore, BSE-SEM was applied to quantitatively analyse an $\text{Al}_{0.22}\text{Ga}_{0.78}\text{N}/\text{GaN}$ -layer system⁸ and to quantify the composition of $\text{In}_x\text{Ga}_{1-x}\text{As}$ layers embedded in a GaAs matrix.⁹ BSE analysis was also utilised to determine layer thicknesses by comparing the measured BSE intensities with MC simulations.^{10,11,12} MC simulations are also often carried out to optimise the BSE image contrast and distinguish features of interest in BSE images. In this way, Kowoll et al.¹³ understood the BSE contrast of complex nanoscale samples such as SiO_2 NPs deposited on indium-tin-oxide-covered glassy carbon substrates. Aoyama et al.¹⁴ studied the BSE contrast of heat-treated steel by controlling the primary electron energy and the detection-angle range. Sato et al.¹⁵ used the BSE-intensity dependence on the detection-angle range to distinguish different phases in steel. Moreover, based on MC simulations, experimental conditions for the separation of topography and material contrast could be derived.¹³ Wan et al.¹⁶ exploited the different angular selectivity of the BSEs to distinguish topography and material contrast of polymer samples.

The quantitative BSE-SEM studies mentioned above include MC simulations as an essential tool to extract quantitative information from the BSE images. In MC simulations, the electron trajectories are traced by a sequence of single scattering events governed by random numbers.

MC-simulated image intensities strongly depend on the used differential scattering cross-section (DSCS) or, in more detail, on the screening parameter in the screened Rutherford cross-section.¹⁷ Suitable DSCSs for MC simulations depend on the material and the experimental conditions.¹⁸ To achieve reliable MC-simulation data, the used MC-simulation software must be first calibrated with the particular material system and experimental setup. Comparing MC-simulated intensities with measurements validate the calibration and enables reliable prediction of BSE contrast as well as optimisation of the imaging parameters. To facilitate the comparison of MC-simulated and measured BSE-SEM intensities, normalisation of the data is necessary because absolute image intensities cannot be compared. The measured BSE intensities can be normalised using, for example, the difference between the maximum and minimum intensity⁶ or using an analytical formula that was previously calibrated to particular conditions.¹⁹

Despite the crucial importance of the MC simulations in the quantitative BSE analyses, not much attention has been paid to the ability of the MC simulations to realistically represent the measured data. In this work, we propose a quantitative BSE method that also relies on the comparison of measured BSE intensities with MC simulations. However, the new method includes additional measures to improve and validate the agreement of the MC simulations with experimental data. We use a wedge-shaped specimen prepared by focused-ion-beam (FIB) milling from the studied bulk material, where the sample thickness gradually increases from 0 to a thickness that represents the bulk case. BSE-SEM images of wedge samples yield BSE-intensity-thickness profiles, which are suitable for comparison with simulated data with the sample thickness as an additional parameter for comparison. Direct comparison is possible by normalising the BSE intensities to the intensity of bulk Si. The bulk Si can be either present in the studied specimen (as a substrate for layer systems) or a Si wafer is utilised for the normalisation. Moreover, we consider the BSE-detector properties in the simulations to improve the agreement with the measured data. The proposed method is tested on two differently challenging multilayer-sample systems. The first is a $\text{ZnS}/\text{Zn}(\text{O}_x\text{S}_{1-x})/\text{ZnO}/\text{Si}$ -multilayer system, where the chemical composition between individual layers varies only slightly and thus probes the sensitivity of the method. The second studied sample is a PTB7/PC₇₁BM-multilayer system, which was chosen as a representative of weakly scattering materials with similar electron-scattering properties. The quantitative analysis of both sample systems demonstrates the validity of the proposed method and emphasises the importance of realistic MC simulations for quantitative BSE-SEM analysis.

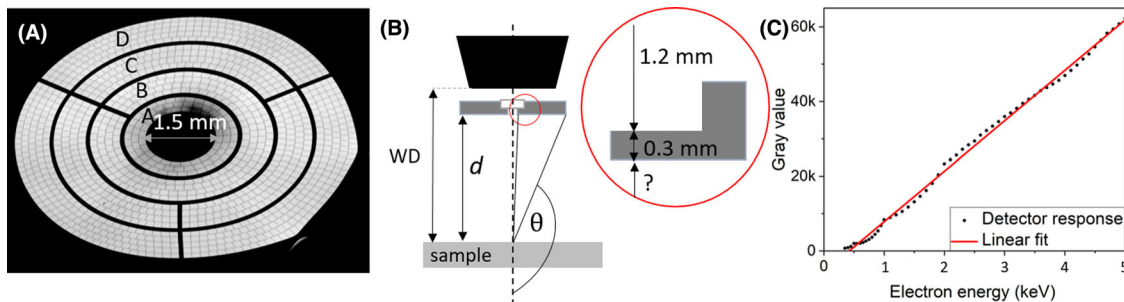


FIGURE 1 CBS-detector properties. (A) Electron-mirror image of the CBS detector, where the image scale can be calibrated with the known size of the bore of the pole piece of 1.5 mm. (B) Scheme of the CBS-detector position in the microscope. The distance between the bottom surface of the detector and the sample surface d is essential for the determination of the collection-angle range of the CBS detector. (C) Measured response curve of the CBS detector. The linear fit of measured data reveals the detector threshold energy $E_{th} = 500$ eV

2 | METHODS

Here we present the proposed quantitative BSE method that is based on the comparison of measured BSE intensities with MC simulations. For realistic MC simulations, the BSE-detector properties (detection-angle range and threshold energy) must be precisely characterised and considered in the MC simulations. Further, the choice of the proper DSCSs used in the MC simulations must be considered. In the proposed method, the measured data are acquired using an electron-transparent wedge-shaped specimen, which introduces the sample thickness as an additional parameter for the comparison with simulations. We use normalisation of the BSE intensities with respect to the Si-bulk intensity, which enables comparison of the measured and simulated data and extraction of the quantitative information. The individual steps of the quantitative method are outlined in the following.

2.1 | Semiconductor detector properties

All experimental data shown in this work were acquired with a Helios G4 FX dual-beam instrument (Thermo Fisher Scientific, USA). The instrument was used in the field-free mode. The beam-convergence angle was 2.83 mrad. This instrument is equipped with an annular semiconductor backscattered-electron (CBS) detector positioned below the pole piece (see Figure 1). Utilising the CBS detector for quantitative BSE analysis is convenient because this detector does not require any electrical and magnetic fields to collect BSEs, and thus the comparison with simulations is feasible. To achieve agreement between measured and simulated data, all experimental parameters (primary electron energy and beam current, detector-collection angles, threshold energy, etc.) must be known. Figure 1A shows an image of the CBS detector, which was acquired using the electron-mirror phenomenon.²⁰ The

TABLE 1 CBS-detector properties

Segment		Radius r (mm)	collection angle θ (rad)
A	Inner	2.4	2.79
	Outer	4	2.59
B	Inner	4.2	2.57
	Outer	6.4	2.36
C	Inner	6.7	2.34
	Outer	9.2	2.19
D	Inner	9.4	2.18
	Outer	12	2.07

Note. The inner and outer radii of the CBS detector segments A–D were determined from a mirror-electron image. The derived collection angles correspond to $WD = 8$ mm

CBS detector consists of four concentric segments labelled A–D. The mirrored image is not scaled; however, calibration with the known size of the bore of the pole piece (1.5 mm) is possible. From the calibrated image, the inner and outer radii (Table 1) of the CBS-detector segments can be determined. To calculate the collection angles for the CBS-detector segments, the distance d between the sample and the detector must be known, as schematically shown in Figure 1B. The working distance (WD) is known and describes the distance between the pole piece and the sample surface. The distance between the pole piece and the surface of the CBS detector (1.2 mm) was determined by focusing the electron beam on the upper side of the CBS detector. The last necessary distance is the thickness of the active semiconductor layer. This thickness was estimated to be 0.3 mm.²¹ The distance d for a particular WD is $d = WD - 1.5$ mm. The collection angles θ for the detector segments A–D result from geometry and are given by Equation (1). The calculated collection angles for $WD = 8$ mm are given in Table 1.

$$\theta = \pi - a \tan \left(\frac{r}{d} \right) [\text{rad}]. \quad (1)$$

The surface of the semiconductor detector is protected by a thin metal layer. As a result, the impinging electrons need to penetrate this layer and lose part of their energy. To consider this effect in the MC simulations, a threshold energy E_{th} is introduced.¹ Electrons with lower electron energy than the E_{th} , that reach the detector, are partially adsorbed in the protection layer and contribute to the calculated BSE intensity with linearly decreasing detection efficiency. E_{th} can be determined by measuring the detector response curve. The response curve describes the dependence of the measured grey values as a function of the primary electron energy. Importantly, the contrast/brightness settings must remain unchanged throughout the whole measurement. For each electron energy, an SEM image of a Si wafer and a corresponding blanked-beam image was acquired. The grey values plotted as a function of primary electron energy in Figure 1C are obtained by subtracting the averaged blanked-beam intensities from the corresponding averaged Si intensities. The response curve shows local maxima at 1 and 2 keV and becomes close to linear for higher electron energies. The origin of these local maxima is not obvious; however, most probably they originate from the detector-amplifier system. Fitting a linear curve to the data shown in Figure 1C reveals an intersection with the energy axis at $E_{th} = 500$ eV, which is the detector threshold energy.

2.2 | Monte–Carlo simulations

In this work, the NISTMonte simulation package²² was used to calculate the properties of BSEs (energy and scattering angle). The simulated BSE intensity I_{MC} is given by the number n_i of BSEs scattered into the collection-angle range of the CBS detector according to Equation (2)

$$I_{MC} = \frac{\sum_{i=1}^{n_i} (E_i - E_{th})}{n_0 (E_0 - E_{th})} \quad (2)$$

with the total number of incident (simulated) electrons n_0 , the primary electron energy E_0 , and the energies E_i of the BSEs emitted from the sample. The MC simulations are typically performed with 10^5 electrons per data point.

Implemented in the NISTMonte simulation package are screened Rutherford differential scattering cross-sections (SR-DSCSs) and the continuous-slowning-down approximation²³ for the calculation of the energy loss and scattering angle of the electrons. The DSCS describes the electron scattering and is thus an important parameter in the MC simulations. The SR-DSCS is given by Equation (3), where the Z denotes the atomic number, θ the scattering

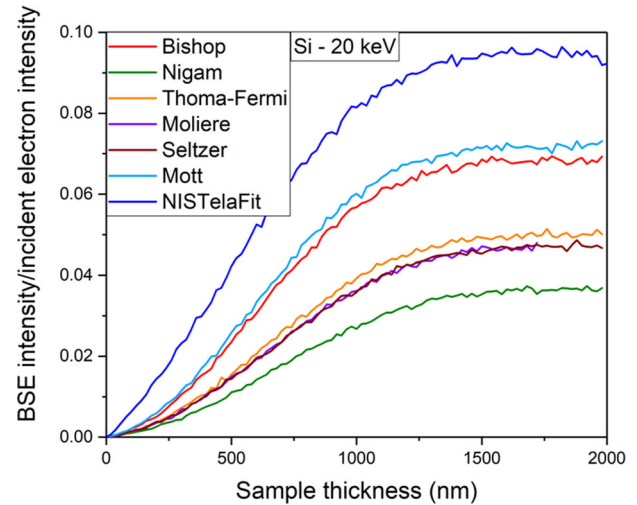


FIGURE 2 BSE-intensity dependence on the DSCS used in the MC simulations. BSE intensity versus thickness curves calculated for silicon at 20 keV electron energy with different screening parameters (see legend) used the SR-DSCS. The light blue curve was calculated using the Mott DSCS

angle and η the screening parameter.

$$\frac{d\sigma}{d\Omega} = \left(\frac{eZ}{4\pi\epsilon_0} \right)^2 \frac{1}{4E_0^2} \frac{1}{(1 - \cos(\theta) + 2\eta)^2}. \quad (3)$$

Several different expressions for η in the SR-DSCSs are available in the literature,²⁴ which yield different MC-simulation results.¹⁷ Suitable DSCSs for MC simulations depend on the material and the experimental conditions.¹⁸ To achieve realistic MC-simulation data, the MC-simulation package must be first calibrated to the particular sample material and experimental setup. To obtain the dependence of the simulated BSE intensity on the sample thickness, the MC simulations were performed in the thickness range between 1 and 3000 nm with 10 nm thickness intervals. By integrating the angular distribution of the backscattered electrons over the complete detection-angle range of the CBS detector from 2.07 to 2.79 mrad (see Table 1), the simulated BSE intensity is calculated at each sample thickness.

We first focus on the BSE intensity of Si from a Si wafer, because the BSE intensity of Si is used in the following to normalise the BSE intensities of our samples of interest. Figure 2 shows the simulated BSE intensity versus thickness curves for Si (the description of the Si specimen is included in the next subsection) using different screening parameters η in the SR-DSCS for a primary electron energy of 20 keV. The applied screening parameters are given in the legend of Figure 2 (see reference Ref. 24). Additionally, the results for the Mott DSCS²⁵ are plotted in light blue.

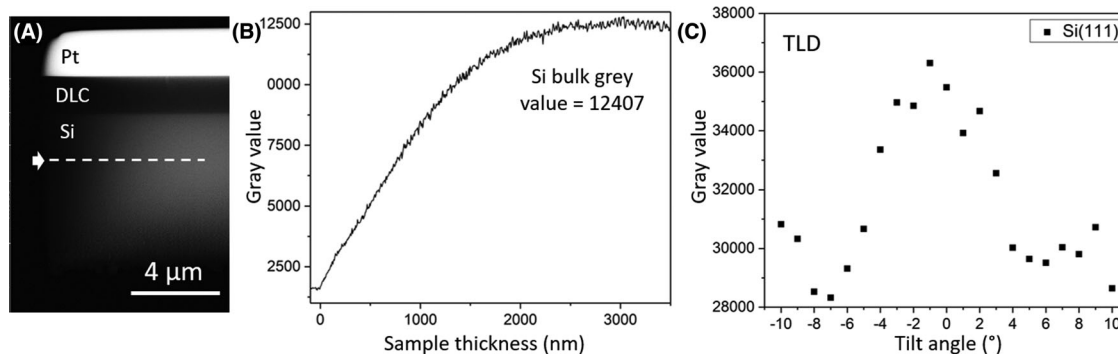


FIGURE 3 Data normalisation by the Si-bulk intensity. (A) 30 keV BSE-SEM image of a FIB-milled wedge-shaped cross-section specimen containing diamond-like carbon (DLC) layer covered with a Pt-protection layer on a Si substrate. (B) An intensity-line profile along the white dashed line in (A) reveals the grey-value dependence on the local sample thickness of the Si wedge. (C) BSE-SEM intensity as a function of the sample orientation. The data were measured on a Si(111) wafer with 2 keV electrons

The curves have a similar shape, that is, the BSE intensity increases with increasing sample thickness because more electrons are backscattered. The BSE intensity saturates when the bulk BSE intensity is reached. Figure 2 reveals that the MC-simulation results depend strongly on η , which can serve as a calibration parameter.

2.3 | Normalisation of BSE-SEM intensities

To enable the comparison of measured intensities with MC simulations, normalisation is necessary. In our approach, we use Si as reference material and normalise the measured BSE intensities with respect to the Si BSE-bulk intensity. Si was chosen because it can be obtained with high purity and is widely used, for example, as a substrate for layer systems.

The proposed quantitative BSE method uses wedge-shaped samples with a known thickness profile, which are prepared from the bulk material according to the following procedure. First, a Pt layer is deposited to protect the material from damage by the Ga^+ ions. A lamella with a thickness of about 1.5 μm is then prepared which is further thinned in a wedge-like shape with a wedge angle α . To obtain a smooth and sharp wedge edge, a small Ga^+ current (63 pA) and low voltage (5 kV) are applied for final polishing. The low-voltage polishing also reduces the Ga^+ implantation on the FIB-milled surface.

Figure 3A shows a 30 keV BSE-SEM image of a wedge-shaped specimen, where a diamond-like carbon (DLC) layer and a Pt-protection layer are deposited on a Si substrate. The wedge thickness increases from left to right and the black regions represent a vacuum. Performing a line scan in the Si substrate along the white dashed line yields the BSE intensity versus thickness curve plotted in Figure 3B. The sample thickness t on the x -axis is obtained from $t = x \tan \alpha$, where x is the distance along the line scan

and α is the wedge angle. The measured line scan does not start from 0 but from a black intensity I_b (intensity of the vacuum), increases with increasing sample thickness and reaches the bulk intensity value $I_{Si\text{bulk}}$. Normalising the measured intensities I_m according to Equation (4), the measured BSE intensity versus thickness curve can be directly compared with MC simulations. Equation (4) contains a geometrical correction factor c_g describing the area percentage of the BSE detector, which does not contribute to the BSE signal. For our system c_g is 0.07 because, as seen in Figure 1A, the detector segments are separated by inactive regions covering 7% of the detector area. If Si is not present in the studied sample as a substrate, $I_{Si\text{bulk}}$ can be obtained from a Si wafer placed next to the sample in the microscope chamber. Using the same imaging parameters (particularly the contrast/brightness settings) as in Figure 3A, the acquired BSE image of a Si wafer (image not shown) yields an average value 12012 for the BSE-bulk intensity. This is very similar to the bulk-Si grey value obtained for the Si wedge. Agreement between the bulk-Si grey values measured on Si wedge and Si wafer was obtained also for 15, 10 and 5 keV. We note that the bulk-Si grey values are similar throughout the whole wafer and that the electron-beam-induced contamination does not have a significant influence on the BSE intensity at primary electron energies between 5 and 30 keV. Moreover, the presence of the native SiO_x on the Si wafer might influence the measured BSE-bulk intensity. The used Si wafer is specified to have a 2 nm thick native SiO_x layer. MC simulations were performed and showed that a 2 nm surface layer of SiO_2 does not significantly influence the bulk-Si BSE intensity at electron energies between 5 and 30 keV.

$$I_{\text{Norm}} = \frac{I_m (1 + c_g) - I_b}{I_{\text{Sibulk}} (1 + c_g) - I_b} \quad (4)$$

The BSE intensity is expected to depend on the crystal orientation of the Si wafer due to electron channelling.²⁶

TABLE 2 Material parameters of the ZnS/Zn(O_xS_{1-x})/ZnO/Si-multilayer system

Material	Average atomic number $Z = \sqrt{\sum_i c_i Z_i^2}$	Density ρ (g/cm ³)	Average atomic mass $A = \sum_i c_i A_i$ (atomic mass units)
ZnO	21.95	5.61	40.69
Zn(O _{0.7} S _{0.3})	22.6	5.15	43.1
Zn(O _{0.5} S _{0.5})	23	4.85	44.71
Zn(O _{0.4} S _{0.6})	23.23	4.7	45.51
ZnS	24	4.09	48.72
Si	14	2.33	28.09

This effect is undesired because we need a robust normalisation method. To investigate the influence of the crystal orientation on the BSE intensity, the Si(111) wafer was tilted while BSE images were acquired for each tilt angle. Figure 3C shows the result, where the grey values were obtained by averaging the BSE intensities for each acquired BSE image. The shape of the curve in Figure 3C shows a peak at -1° tilt and minima around -7° and 6° . The measured data could be the result of the superposition of electron channelling and the sample-tilt dependence of η within the detection-angle range. According to Reimer,¹ the influence of the sample tilt on η at small-angle tilts is insignificant. Therefore, the grey-value modulations in Figure 3C must be induced by channelling. The intensity minima correspond to half of the Bragg angles for the Si(022) planes. Despite the intensity modulations in Figure 3C, we conclude that the sample orientation does not strongly affect the measured BSE intensity and the Si wafer can serve as a robust reference sample for the normalisation of the measured BSE intensities.

2.4 | Applications

2.4.1 | Composition analysis of a ZnS/Zn(O_xS_{1-x})/ZnO/Si-multilayer system

The first test sample to demonstrate the feasibility of the proposed quantitative BSE method is a multilayer system consisting of 100 nm thick layers of ZnS, Zn(O_{0.4}S_{0.6}), Zn(O_{0.5}S_{0.5}), Zn(O_{0.7}S_{0.3}) and ZnO deposited on a Si substrate, as shown in a cross-section scheme in Figure 4A. More details about the sample fabrication are discussed in a publication by Jin et al.²⁷ This particular sample was chosen because the rather small composition variations between the layers probe the sensitivity limits of the suggested quantitative BSE method. Moreover, the material parameters of ZnO and ZnS are well known and yield accurate MC-simulated data. The material parameters of the individual layers are summarised in Table 2. The average atomic numbers and average atomic masses were calculated using formulas shown in Table 2, where c_i are

concentrations of the particular element in the compound in at.%. The material densities for ZnO²⁸ (5.61 g/cm³) and for ZnS²⁹ (4.09 g/cm³) are known and the material densities for Zn(O_xS_{1-x}) were interpolated.

Before the measurement, MC simulations were used to optimise the imaging parameters to achieve the best possible contrast and distinguish the layers in the ZnS/Zn(O_xS_{1-x})/ZnO/Si-multilayer system in BSE-SEM images. The MC simulations for the materials present in the ZnS/Zn(O_xS_{1-x})/ZnO/Si-multilayer system were performed using the Bishop screening parameter³⁰ and the BSE-detector collection angles corresponding to WD = 8 mm (see Table 1). The justification for using the Bishop screening parameter will be given below. Figure 4 compares the MC-simulated BSE intensities for the different materials as a function of the specimen thickness at different primary electron energies. At 2 and 5 keV (Figure 4B and C, respectively), the simulated intensities are similar and do not predict any significant contrast between the different layers. At 15 keV (Figure 4D) in the bulk region ($t > 400$ nm), the curves are also almost identical and, therefore, no contrast is expected. However, at smaller sample thicknesses (highlighted in Figure 4D), MC simulations predict weak contrast between the layers. Despite its lower average atomic number, we note that ZnO appears brighter than ZnS with its low material density. Analysing the specimen at $E_0 > 15$ keV is not convenient because data normalisation using the Si substrate is not possible, because the Si-bulk intensity is not reached at these electron energies for the analysed lamella with a maximum thickness of 1.5 μ m. Figure 4D also contains not only simulated (black curve) but also experimental (red curve) data for Si. Good agreement is observed if the MC simulations are performed with the Bishop screening parameter. Only a small discrepancy is observed at sample thicknesses, where the BSE intensity starts to saturate. The origin of this discrepancy and the acquisition of the experimental Si data is described in context with Figure 5.

The contrast between the layers is determined by the different η of the materials with contributions of electron-beam spreading. For small electron energies and not-too-small specimen thicknesses, the size of interaction volume

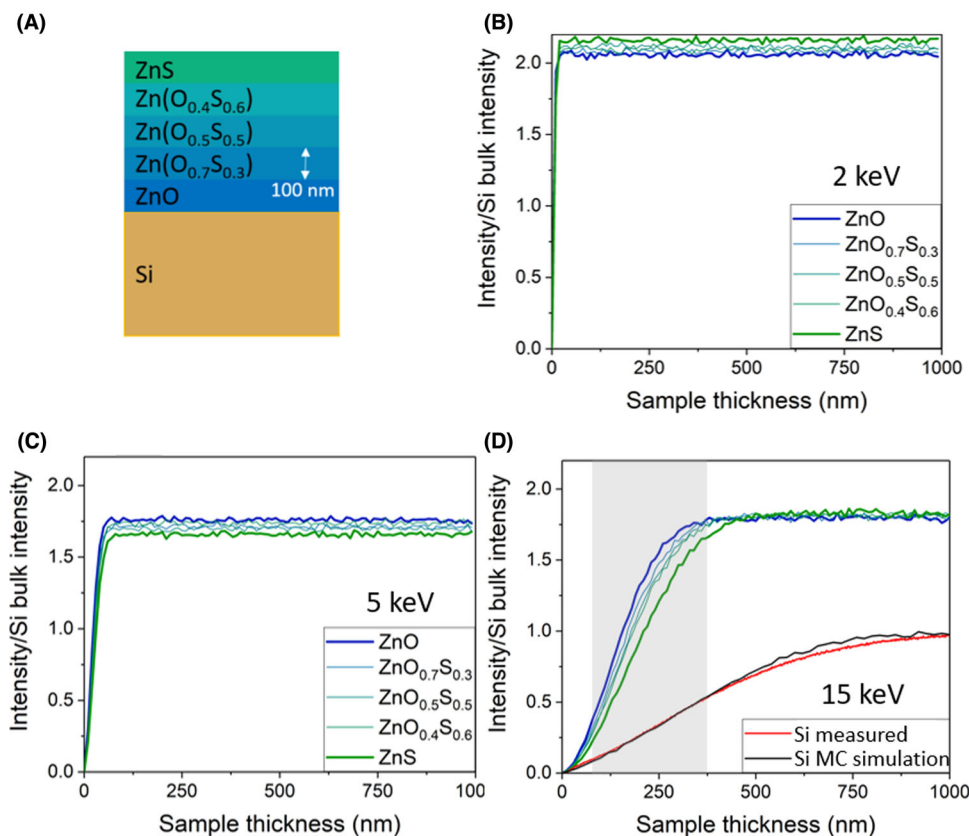


FIGURE 4 MC simulations of the ZnS/Zn(O_xS_{1-x})/ZnO/Si-multilayer system. (a) Cross-section scheme of the ZnS/Zn(O_xS_{1-x})/ZnO/Si-multilayer system with layer thicknesses of 100 nm and the respective chemical compositions. MC-simulated BSE intensity versus sample-thickness curves for the individual layers (colour-coded) are simulated at (B) 2 keV, (C) 5 keV and (D) 15 keV. In (D) the measured (red) and MC-simulated (black) BSE intensity versus thickness curves for Si are additionally displayed

is relevant because it will be completely contained in the specimen. For a layer system, the size of the interaction volume needs to be considered with respect to the layer thickness of only 100 nm. For comparatively large electron energies and not-too-large specimen thicknesses, the interaction volume is only partially contained in the specimen. In this case, it is more appropriate to consider beam broadening. For a layer system, the maximum specimen thickness depends on the layer thickness and the used (high) electron energy. The size of the interaction volume increases with increasing electron energy and can be estimated using Equation (5),³¹ where E_0 is the primary electron energy in keV and ρ is mass density in g/cm³.

$$R = 40 \frac{E_0^{1.75}}{\rho} \text{ (nm)}. \quad (5)$$

With respect to the layer thicknesses of 100 nm in the ZnS/Zn(O_xS_{1-x})/ZnO/Si-multilayer system, it is important to note that the interaction volumes of ZnS and ZnO are 164 and 119 nm, respectively, already at a small electron energy of 5 keV. Only negligible contrast is predicted at 5 keV and below (Figure 4B and C) and it is indeed rea-

sonable to perform the analysis at 15 keV at small sample thicknesses as suggested by Figure 4D. Since the size of the interaction volume at 15 keV is much larger than the sample thickness ($R_{\text{ZnS}} = 1120\text{nm}$ and $R_{\text{ZnO}} = 815\text{nm}$), beam broadening must be considered here. The beam broadening can be estimated by Equation (6),³² where Z is the average atomic number of the sample with thickness t in units of cm and average atomic weight A in g/mol.

$$b = 625 \frac{Z}{E_0} \sqrt{\frac{\rho}{A}} t^{3/2} \text{ (cm)}. \quad (6)$$

The experimental data in the following (Figures 5 and 6) were acquired at a specimen thickness of 110 nm, where sufficient contrast is expected. Beam broadening for 15 keV and 110 nm specimen thickness is 105 nm for ZnS and 124 nm for ZnO, which is only slightly above the layer thicknesses of 100 nm. Larger specimen thickness will increase the effect of beam broadening leading to broadened intensity transition between the layers.

Based on MC simulations (Figure 4), the layers in the ZnS/Zn(O_xS_{1-x})/ZnO/Si-multilayer system can be best distinguished for 15 keV electron energy and small sample

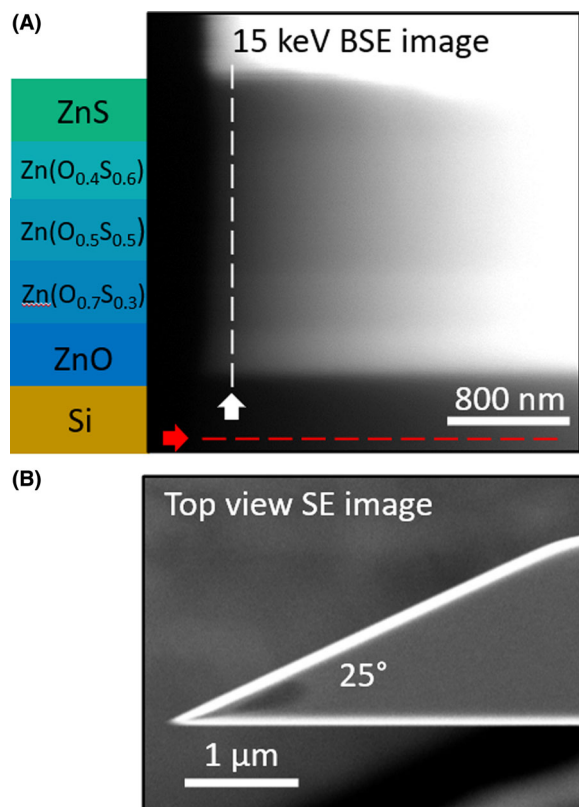


FIGURE 5 BSE-SEM imaging of the ZnS/Zn(O_xS_{1-x})/ZnO/Si-multilayer system. (A) 5 keV top-view secondary-electron SEM image of the FIB-milled wedge, from which the wedge angle was measured. (B) 15 keV BSE-SEM cross-section image of the wedge, which was acquired by using all segments of the CBS detector at 8 mm WD. The thickness increases from left to right and the ZnS/Zn(O_xS_{1-x})/ZnO-multilayer system is between the Pt-protection layer and the Si substrate as indicated by the scheme

thicknesses. We note that changing the collection-angle range of the CBS detector (by adjusting the WD) does not improve the contrast between the layers.

Experimental BSE-SEM images were acquired using a FIB-prepared wedge specimen of the ZnS/Zn(O_xS_{1-x})/ZnO/Si-multilayer system that was prepared according to the procedure described above. A top-view secondary-electron SEM image of the wedge (Figure 5A) enables the determination of the wedge angle, which is $\alpha = 25^\circ$. A cross-section view is obtained by tilting the sample by 90° from the top-view orientation. Figure 5B shows a 15 keV BSE-SEM cross-section image acquired with the CBS detector at 8 mm WD. The top layer with bright contrast represents the Pt-protection layer, underneath is the ZnS/Zn(O_xS_{1-x})/ZnO-multilayer system, and at the bottom is the Si substrate with dark contrast. The wedge thickness increases from left to right and the vacuum region to the left displays black contrast. The BSE intensity as a function of the specimen thickness for Si (see

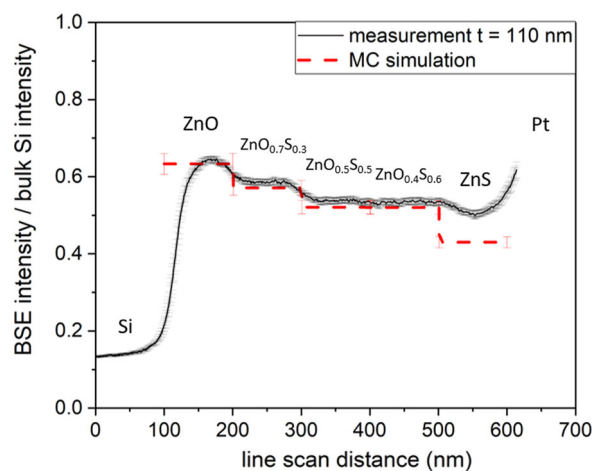


FIGURE 6 Comparison of measured and simulated normalised BSE intensities for the ZnS/Zn(O_xS_{1-x})/ZnO/Si-multilayer system. The black curve represents the measured 15 keV BSE intensity-line profile perpendicular to the ZnS/Zn(O_xS_{1-x})/ZnO/Si-multilayer system from Figure 5B at 110 nm wedge thickness. The red-dashed curve shows the MC-simulated data using the Bishop screening parameter

Figure 4D) is obtained by performing a 20 pixel-wide line scan along the red-dashed line in Figure 5B. Normalising the BSE intensities to the Si bulk intensity according to Equation (4) enables the comparison with MC simulations (Figure 4D). A small discrepancy between experimental and simulated BSE intensities is observed at sample thicknesses, where the BSE intensity starts to saturate. The origin of the discrepancy could be related to the imprecisely determined wedge angle of the wedge sample. The wedge angle is determined from a top-view secondary-electron SEM image where only the Pt-protection layer is visible. The wedge angle for the multilayer system below could slightly differ from the wedge angle measured for the Pt-protection layer due to different sputtering rates for the different materials. Accordingly, the calculated sample thicknesses for the line scan in the Si substrate could be slightly different.

The individual layers of the ZnS/Zn(O_xS_{1-x})/ZnO-multilayer system can be distinguished in the 15 keV BSE image in Figure 5B with weak contrast as suggested by the MC simulations in Figure 4D. To minimise the effect of beam broadening, an intensity-line scan perpendicular to the ZnS/Zn(O_xS_{1-x})/ZnO-multilayer system was performed in the thinnest region of the wedge sample along the white dashed line in Figure 5B. The measured BSE intensities (Figure 6, black line) are normalised according to Equation (4). For comparison with MC simulations, the precise wedge thickness at the position of the line scan must be known and can be determined from the Si intensity by comparison with MC simulations. The

normalised BSE intensity at the beginning of the line scan (black curve in Figure 6) corresponds to Si and has a value of 0.13. According to Figure 4D, the normalised intensity of 0.13 corresponds to the BSE intensity of Si with a thickness of 110 ± 10 nm. The uncertainty represents the discrepancy between the measured and simulated data in Figure 4D. The main error for the experimental data in Figure 6 originates from the acquisition of the line scans. The line scan should be oriented exactly perpendicular to the wedge thickness gradient. In practice, this is challenging, and therefore an error bar is given for the measured data obtained by performing five line scans at the same sample thickness and calculating the standard deviation for the average value. In Figure 6, the MC-simulated BSE intensities with the Bishop screening parameter are plotted for a specimen thickness of 110 nm by a dashed-red line. The error of the simulated data is estimated from the Poisson noise in the MC simulations.

Apart from ZnS, the contrast of the experimental data agrees well with the MC simulations. The different layers in the ZnS/Zn(O_xS_{1-x})/ZnO-multilayer system can be clearly distinguished with the exception of the Zn(O_{0.5}S_{0.5}) and Zn(O_{0.4}S_{0.6}) layers, where the chemical composition is too similar. The measured intensity is in general slightly higher than the MC-simulated data. This small discrepancy could originate from Ga⁺ implantation. Even though measures to minimise Ga⁺ implantation were applied, implantation of some Ga⁺ is inevitable. In general, the presence of Ga⁺ ions would increase the measured BSE intensity of the ZnS/Zn(O_xS_{1-x})/ZnO-multilayer system and thus can cause the small discrepancy in Figure 6. For the ZnS layer, the simulations and measured data do not agree well. The discrepancy can be explained by considering beam broadening in the experimental data. The ZnS layer is located next to the Pt-protection layer on right in the line scan in Figure 6. Beam broadening for ZnS is 105 nm at 110 nm specimen thickness according to Equation (6), which leads to a significant contribution of BSEs from the strongly scattering Pt-protection layer. The influence of the beam broadening is also visible in the measured data for ZnO, where the ZnO intensity decreases towards the intensity of Si and is reduced compared to the simulated BSE intensity of ZnO.

Figure 6 reveals that the proposed approach for quantitative BSE analyses is adequate. By analysing a wedge-shaped specimen, the determination of the O and S contents in ZnS/Zn(O_xS_{1-x})/ZnO-multilayer system is possible in thin sample regions. This material system is particularly challenging because, in addition to small composition differences, the small layer thicknesses of 100 nm impose further constraints on contrast optimisation because the size of the interaction volume and beam broadening must be considered. The MC-simulated BSE

intensity versus thickness curves, calculated by using the Bishop screening parameter, describe the measured data well and can be applied for reliable optimisation of the imaging parameters. Moreover, the ZnS/Zn(O_xS_{1-x})/ZnO-multilayer system provides information on the limits of the BSE analysis. It has been shown that materials varying only slightly in chemical composition, for example, Zn(O_{0.7}S_{0.3}) and Zn(O_{0.5}S_{0.5}), can be distinguished in a BSE-SEM image if the interaction volume is not relevant at small sample thicknesses. However, materials with chemical compositions as close as Zn(O_{0.5}S_{0.5}) and Zn(O_{0.4}S_{0.6}) cannot be distinguished because the scattering properties of the two materials are almost identical.

2.4.2 | PTB7/PC₇₁BM-multilayer system

A PTB7 (C₄₁H₅₃FO₄S₄) / PC₇₁BM (C₈₂H₁₄O₂) multilayer system was analysed as 2nd test sample because it represents weakly scattering materials with similar scattering properties. The PTB7/PC₇₁BM multilayer system consists of alternating layers of pure PTB7 and pure PC₇₁BM with thicknesses between 160 and 320 nm stacked on a Si substrate. The Si substrate was used to normalise the measured BSE intensities of PTB7 and PC₇₁BM. Information on the sample fabrication can be found in a publication by Li et al.³³ From the bulk sample, a wedge-shaped lamella with a wedge angle of 25° was prepared by FIB milling using the procedure described above.

The layer structure of the PTB7/PC₇₁BM test sample is schematically shown in Figure 7A. In Figure 7B, a cross-section high-angle annular dark-field scanning transmission electron microscopy (HAADF-STEM) image of the FIB-prepared PTB7/PC₇₁BM wedge is shown that was acquired at 30 keV and 0.4 nA electron beam current with the STEM detector implemented in the Helios microscope, which covers a detection-angle range from 65 to 272 mrad. HAADF-STEM imaging was used to verify the arrangement of the PTB7 and PC₇₁BM layers in the sample because the HAADF-STEM contrast of PTB7 and PC₇₁BM is already well understood.³³ In Figure 7B, the wedge thickness increases from left to right. In the thin sample regions, PC₇₁BM shows brighter contrast compared to PTB7. At a thickness $t \approx 475$ nm, a contrast inversion occurs (marked by a white dashed line) and for larger thicknesses, PTB7 shows brighter contrast than PC₇₁BM. From the HAADF-STEM image in Figure 7B, the PTB7 and PC₇₁BM layer thicknesses can be measured. Moreover, Figure 7B shows several bright few-nm thick lines within the PTB7/PC₇₁BM-multilayer system, marked by red arrows in Figure 7B (red lines in Figure 7A). These bright lines correspond to thin PEDOT(C₆H₄O₂S):PSS(C₈H₈O₃S) layers, which are remnants from sample fabrication.³³

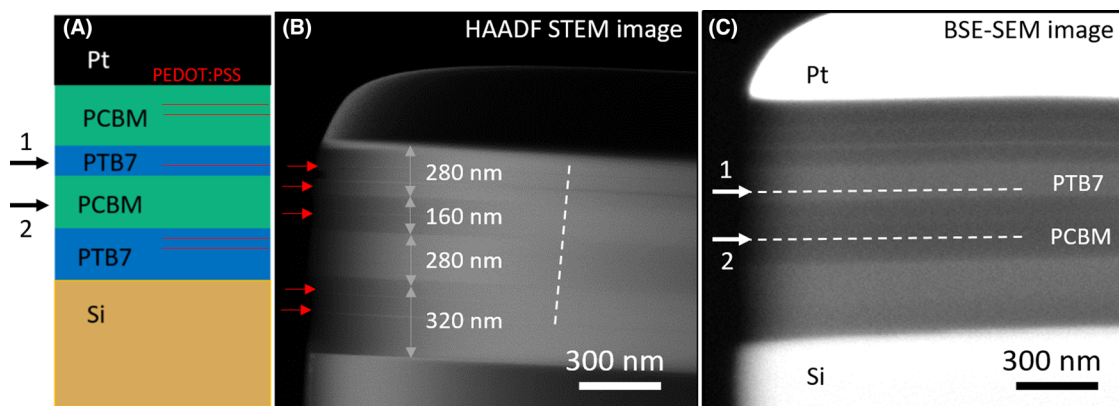


FIGURE 7 Scheme, HAADF-STEM and BSE-SEM images of the PTB7/PC₇₁BM-multilayer system. (A) The scheme of the PTB7/PC₇₁BM-multilayer system in a cross-section perspective shows the arrangement of the layers. (B) 30 keV HAADF-STEM image of the FIB-prepared wedge-shaped specimen with the same layer sequence as in (A). The typical contrast inversion between the PTB7 and PC₇₁BM layers with increasing specimen thickness is marked by the white dashed line. Additional thin PEDOT:PSS layers are present, marked by red arrows in (B) and by red lines in (A), which are an artefact from the fabrication process. (C) 5 keV BSE-SEM image of the PTB7/PC₇₁BM-multilayer system wedge specimen

TABLE 3 Material parameters of the PTB7/PC₇₁BM-multilayer system

Material	Chemical formula	Average atomic number $Z = \sqrt{\sum_i c_i Z_i^2}$	Density ρ (g/cm ³)	Average atomic mass $A = \sum_i c_i A_i$ (atomic mass units)
PTB7 ³⁷	C ₄₉ H ₅₇ FO ₄ S ₄	5.26	1.17	2.73
PC ₇₁ BM ⁴⁰	C ₈₂ H ₁₄ O ₂	5.62	1.63	3.24
PEDOT:PSS ^{39,38}	(C ₆ H ₄ O ₂ S): (C ₈ H ₈ O ₃ S)	6.39	1.18	9.82

Table 3 lists the material parameters of the PTB7/PC₇₁BM-multilayer system that were used in the MC simulations. The small differences in the average atomic numbers, the material densities and the average atomic masses indicate that the contrast will be weak. Hence, MC simulations were carried out to determine the best imaging conditions to obtain the best contrast between the PTB7 and PC₇₁BM. It was found that the Bishop screening parameter (well suited for the ZnS/Zn(O_xS_{1-x})/ZnO-multilayer system) does not adequately describe the experimental BSE-SEM intensities of the PTB7/PC₇₁BM-multilayer system. The best agreement between the measured and MC-simulated data was obtained for the NISTelaFit screening parameter³⁰ (data not shown here), which is also implemented in the NISTMonte software. Hence, only MC simulations using the NISTelaFit screening parameter are displayed in the following. MC simulations were performed for the isolated materials and, in addition, at electron-beam positions 1 and 2 (see Figure 7A) taking the complete structure of the PTB7/PC₇₁BM-multilayer system including the Pt-protection layer into account.

MC-simulated BSE intensity versus thickness curves for WD = 8 mm at different electron energies are dis-

played in Figure 8. The dashed curves correspond to the MC-simulated data for PTB7 at position 1 (black-dashed lines) and for PC₇₁BM at position 2 (red-dashed lines). Additionally, BSE intensity versus thickness curves calculated for isolated PTB7 (full black lines) and PC₇₁BM (full red lines) are displayed. By comparing the colour-coded dashed and full lines in Figure 8, the contribution of the surrounding layers can be recognised due to the influence of beam broadening and interaction volumes. At 2 keV (Figure 8A), the full and dashed lines coincide indicating that the interaction volume does not exceed the thickness of the PTB7 (or PC₇₁BM) layer and that the surrounding layers of the PTB7/PC₇₁BM-multilayer system do not contribute to the simulated PTB7 (or PC₇₁BM) BSE intensity. This is consistent with the calculated size of the interaction volume (according to Equation 5) for PC₇₁BM (42 nm) and PTB7 (58 nm). At 5, 10 and 15 keV electron energies (Figure 8B–D), the adjacent layers contribute to the simulated BSE intensity leading to an increasing discrepancy between the full and dashed lines at increasing specimen thicknesses.

The contrast between the PTB7 and PC₇₁BM layers is given by the difference between the red and black curves.

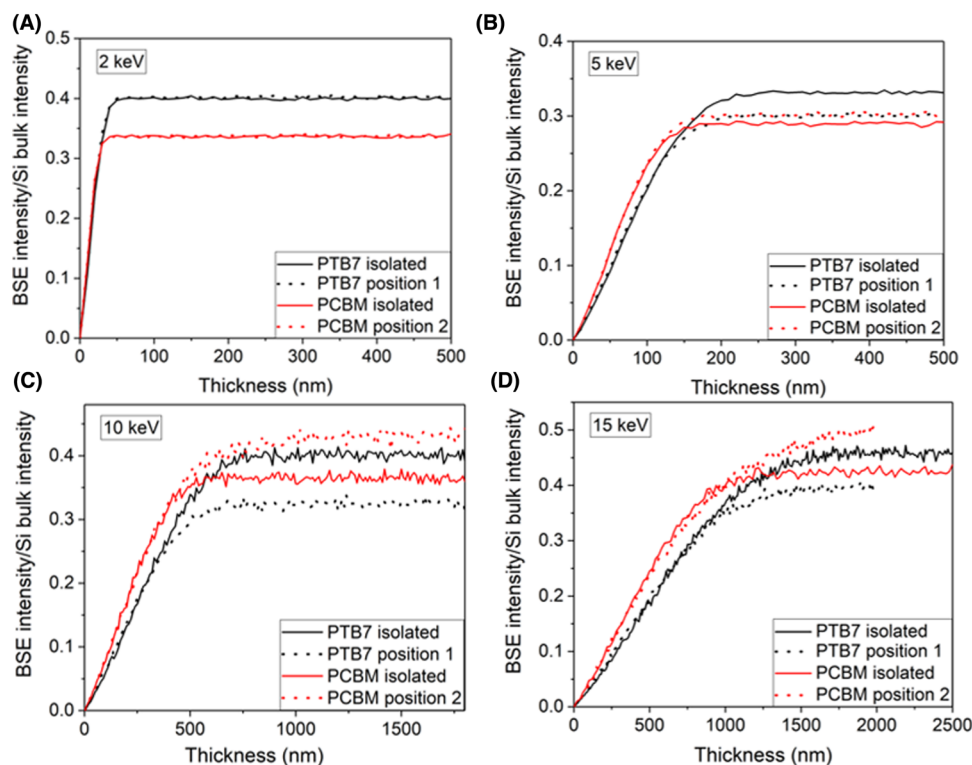


FIGURE 8 MC simulations for the PTB7/PC₇₁BM-multilayer system. MC-simulated BSE intensity versus thickness curves for isolated PTB7 (full black lines) and PC₇₁BM (full red lines). The corresponding dashed colour-coded PTB7 and PC₇₁B curves represent the BSE intensities for the incident electron beam positioned on the PTB7 and PC₇₁B layers in the PTB7/PC₇₁BM-multilayer system. The curves are compared at (A) 2 keV, (B) 5 keV, (C) 10 keV and (D) 15 keV primary electron energies

According to the MC-simulated data in Figure 8, the highest contrast is expected for the bulk region and therefore we will focus only on the bulk case. We note, that PTB7 shows brighter contrast than PC₇₁BM at all studied electron energies for isolated materials (full lines in Figure 8). Considering the contribution of the surrounding layers to the simulated BSE intensity (dashed lines) the situation is more complex. At 5 keV (Figure 8B) the red and black-dashed lines coincide, and no contrast is expected. At 5 keV, the interaction volume (Equation 5) is already significantly larger than the layer thicknesses and leads to the reduction of the PTB7 bulk intensity by the contribution of the surrounding PC₇₁BM layers. In analogy, the PC₇₁BM bulk intensity is increased by the surrounding PTB7 layers. This effect is even more pronounced at 10 and 15 keV with even larger contributions from the neighbouring layers. Besides the influence of the interaction volume, the escape probability of the scattered electrons from the different materials in the PTB7/PC₇₁BM-multilayer influences the simulated/measured BSE intensity. As a result, weakly scattering materials (PTB7 and PC₇₁BM) contribute more to the simulated/measured BSE intensity than Pt, because the escape probability for these materials is higher compared to Pt.¹ By considering the large interaction volume and the BSE escape probability, the contrast inversion

between the PTB7 and PC₇₁BM at 10 and 15 keV (Figure 8C and D) can be understood. Moreover, PTB7 (black-dashed lines in Figure 8C and D) shows an even lower bulk intensity compared to the bulk intensity for the isolated PC₇₁BM (full red curves in Figure 8C and D). This indicates that, in addition to the effects of the neighbouring layers, a significant number of electrons are scattered into the Pt-protection layer. These electrons are absorbed due to the low escape probability and therefore do not contribute to the simulated PTB7 intensity. This effect is particularly pronounced for the PTB7 layer (position 1 in Figure 7A) with the Pt-protection layer in the vicinity.

Based on the insight into the contrast formation in the PTB7/PC₇₁BM-multilayer system by MC simulations, the most suitable electron energy is 2 keV. At this electron energy, the interaction volume does not exceed the PTB7 and PC₇₁BM layer thicknesses and the interpretation of the image contrast is straightforward. At higher electron energies (5, 10 and 15 keV), the interaction volume exceeds the PTB7 (or PC₇₁BM) layer thickness and significantly influences the BSE intensities leading to a complex situation that is less suitable for quantitative BSE analysis.

To obtain experimental BSE intensity versus thickness curves, a wedge-shaped specimen was prepared by FIB milling according to the procedure described above. An

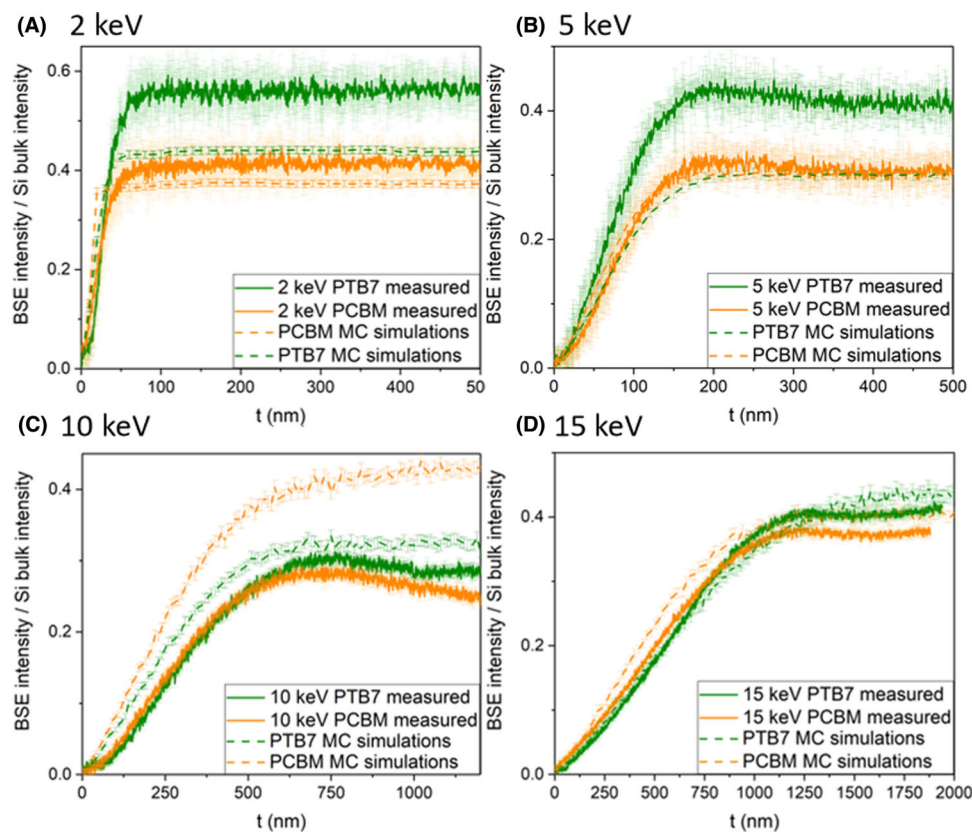


FIGURE 9 Comparison of measured and MC-simulated BSE intensities as a function of the specimen thickness. Comparison of measured and MC-simulated BSE intensities normalised to the Si-bulk intensity as a function of the specimen thickness ($WD = 8$ mm) for (A) 2 keV, (B) 5 keV, (C) 10 keV and (D) 15 keV with measured/simulated data for PTB7 (full/dashed green lines) and measured/simulated data for PC₇₁BM (full/dashed orange line). The MC simulations were performed using the NISTelaFit screening parameter

example of a BSE-SEM image of the prepared PTB7/PC₇₁BM wedge is presented in Figure 7C. The image was acquired with the typical detection-angle range (2.07 to 2.79 rad), corresponding to all segments of the CBS detector and $WD = 8$ mm. In the BSE image, the PEDOT:PSS layers are visible with bright contrast (mainly in the PC₇₁BM layers). Performing 20-pixel-wide intensity-line scans along the white dashed lines in the direction of the arrows in Figure 7C in the PTB7 and PC₇₁BM layers yields the BSE intensity as a function of the sample thickness. The intensity-line scans were performed in the middle of the PTB7 and PC₇₁BM layers to minimise the effect of the neighbouring layers. Each line scan was performed 5 times (at slightly different positions), and the average intensities and the errors were calculated. The BSE intensities normalised with the bulk intensity of the Si substrate are shown in Figure 9.

Figure 9 compares the measured and simulated (considering the surrounding layers) BSE intensities at (A) 2 keV, (B) 5 keV, (C) 10 keV and (D) 15 keV as a function of the specimen thickness for PTB7 (full and dashed green lines) and PC₇₁BM (full and dashed orange lines). We will focus on the bulk case, where the contrast is more pronounced

than at small specimen thicknesses. Figure 9 reveals that the measured PTB7 bulk intensity (green curves) is higher than the PC₇₁BM bulk intensity (orange curves) at all electron energies. In contrast, the situation for MC-simulated data is more complex, as already discussed in Figure 8. At 2 keV (Figures 9A), the MC-simulated curve for PC₇₁BM (dashed orange curve) agrees with the measured PC₇₁BM curve (full orange curve) within the error bars, while the MC-simulated bulk intensity of PTB7 is 25% lower than the measurement. At 15 keV (Figure 9D), the agreement between the measured and simulated BSE intensities is rather good but the contrast is small. At 10 keV (Figure 9C), the measured and simulated PTB7 curves agree reasonably well, whereas the discrepancy is large for PC₇₁BM. Moreover, the bulk intensity for both measured curves is not constant but decreases slightly with increasing sample thickness.

It can be concluded from Figures 8 and 9 that the most suitable electron energy for reliable quantitative BSE analysis of the PTB7/PC₇₁BM-multilayer system (with the given layer thicknesses) is 2 keV, where the contribution of the surrounding layers is minimised due to the small interaction volume and the distinct contrast between the

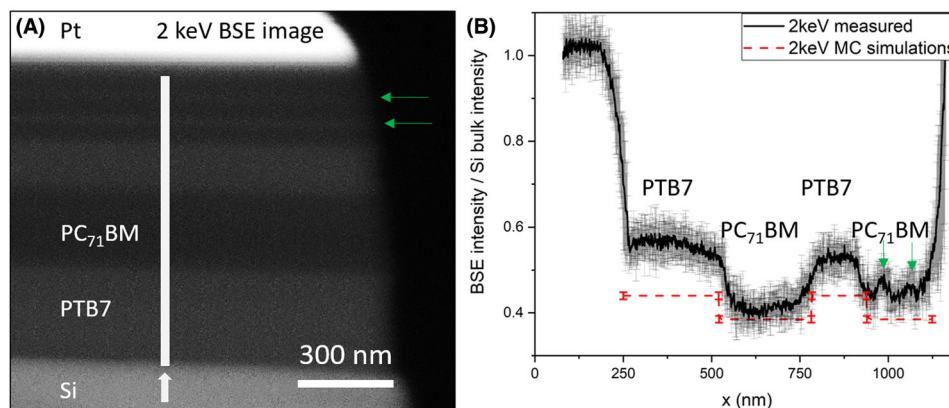


FIGURE 10 BSE-SEM intensity-line scans perpendicular to the PTB7/PC₇₁BM-multilayer system. (A) 2 keV BSE image showing the position of the BSE-intensity line scan across the PTB7/PC₇₁BM-multilayer system. (B) Normalised BSE-intensity line scan (black curve) from (A) and corresponding MC-simulated bulk intensities (dashed-red line). The green arrows indicate PEDOT:PSS layers in (A) and (B)

materials. For the higher electron energies, the situation is more complex because the interaction volume increases strongly and contributions from the whole layer system are expected. Especially contributions from the strongly scattering Pt-protection layer and the Si substrate may not have been properly calculated in the MC simulations of the whole layer system because the NISTelaFIT screening parameter was used for all materials. The (dis)agreement between simulations and measurements may also depend very much on the specific sample region that was analysed. Further reasons are discussed in context with Figure 10.

In Figure 10A, a 2 keV BSE image of the PTB7/PC₇₁BM-multilayer system is presented. Performing a 20-pixel-wide line scan in the bulk region perpendicular to the layer system (along the white line in the bulk region) yields the BSE-intensity profile shown in Figure 10B. The BSE intensities in Figure 10B are normalised by the bulk intensity of the Si substrate. Figure 10B clearly shows the ability of BSE-SEM imaging to distinguish PTB7 and PC₇₁BM. Figure 10B also presents the MC-simulated BSE-bulk intensities by a red-dashed line. The bright PTB7 and dark PC₇₁BM contrast is in qualitative agreement with the simulations. However, the simulated intensities are lower than the experimental data as already observed in Figure 9A. The discrepancy for PC₇₁BM is within the error bars in contrast to PTB7, where the discrepancy is larger. The gradual intensity transitions between the layers are due to the finite size of the interaction volume, which leads to the contribution of the neighbouring layers in the vicinity of the interfaces.

The origin of the discrepancy between the measured and simulated data for PTB7 in Figure 10B is not obvious. Possible reasons could be Ga⁺ implantation as a wedge-preparation artefact during FIB milling, surface contamination, or the MC simulations due to incorrect material parameters. The latter could apply in particular

to the polymer PTB7, while the fullerene-based PC₇₁BM is less likely to show deviations from the literature values.

During the FIB milling of the wedge, measures to minimise the Ga⁺ implantation were applied (5 keV final polishing and grazing incidence angles), which substantially reduce the amount of implanted Ga⁺.³⁴ Despite the final low-energy polishing, some Ga⁺ is inevitably implanted and can increase the measured BSE intensity of the PTB7. The influence of the Ga⁺ implantation on the BSE intensity can be examined by comparison of the measured and simulated BSE intensities for Si. In Figure 4D, the measured (red) and simulated (black) Si curves are compared. We note that the data shown in Figure 4D were derived from a different wedge sample but the wedge-preparation procedure was the same. The Ga⁺ implantation should increase the slope of the measured curve compared to the simulations at small sample thicknesses. However, the measured and simulated curves agree very well in the small sample-thickness region in Figure 4D, indicating that the Ga⁺ implantation is not severe and the influence on the measured BSE intensity is not significant. For the BSE intensities of the weakly scattering PTB7 and PC₇₁BM, the influence of the Ga⁺ implantation is more pronounced and could explain the small discrepancy between the measured and simulated data for PC₇₁BM (Figure 10B). However, the discrepancy for PTB7 is too large to be assigned only to Ga⁺ implantation.

The next possible source for the discrepancy could be surface contamination on the examined wedge specimen. However, this is unlikely because the wedge was FIB milled and the BSE images were acquired directly afterward without exposing the sample to ambient conditions. Moreover, the contamination induced by the electron beam was examined by comparing the measured BSE intensities of the first and last BSE image within the

measurement session, which showed only marginal differences. Hence, it can be concluded that the dependence of the measured BSE intensity on the surface contamination is insignificant.

Another reason for the discrepancy could be the material parameters for PTB7 (Table 3) that were used in the MC simulations. By varying the PTB7 material density between 1.12 and 1.8 g/cm³ in the MC simulations, it was found that the MC-simulated BSE-bulk intensity has the same value in this density range at 2 keV. This can be explained in analogy to BSE-intensity dependence on the sample thickness. The BSE intensity increases with increasing sample thickness because a larger part of the interaction volume is contained in the specimen, and more electrons are backscattered. With the further increase of the sample thickness, the BSE intensity saturates because the penetration depth does not further increase and reaches its maximum value. By increasing the material density, the mean penetration depth decreases and tends to saturation at smaller sample thicknesses with bulk BSE intensities remaining the same for a given electron energy. In addition, the dependence of the PTB7 bulk intensity on the chemical composition (atomic number) was studied. In the MC simulations, two additional sulphur atoms (C₄₉H₅₇FO₄S₆) were added to the nominal chemical composition of the PTB7 molecule (C₄₉H₅₇FO₄S₄). At 2 keV, the simulated BSE-bulk intensity normalised to the Si-bulk intensity yields 0.5 for C₄₉H₅₇FO₄S₆. Comparing this value with the measured intensity of 0.55 and MC-simulated intensity of 0.4 for the nominal PTB7 composition shows an improved agreement between the measurements and simulations at 2 keV. Therefore, it is likely that differences between the nominal and real chemical composition of PTB7 contribute to the discrepancy between the measured and MC-simulated BSE intensities in Figures 10B and 9. The difference between the nominal and real chemical composition of PTB7 could be caused by electron/ion-beam-induced damage. Shrinkage and mass loss caused by electron-beam irradiation was indeed reported for PTB7.^{35,36} PC71BM was found to be more stable under electron-beam irradiation,³⁶ which agrees with our findings because the agreement between measured and MC-simulated data is much better than for PTB7 not only in Figure 10B but also in Figure 9.

3 | SUMMARY

In this work, we have presented a new method for the quantitative analysis of the BSE contrast in SEM. The proposed method is based on the comparison of MC-simulated and measured BSE intensities acquired on wedge-shaped electron-transparent specimens. The known thickness

profile of the wedge specimens provides an additional parameter for quantitative comparison. To enable the comparison of measured and MC-simulated BSE intensities, we propose normalisation of the BSE intensities with respect to the Si-bulk BSE intensity. Moreover, the detector properties must be accurately known and taken into account in the MC simulations to achieve agreement with the measurements.

The feasibility of the proposed BSE method was demonstrated by the analysis of two multilayer samples. The ZnS/Zn(O_xS_{1-x})/ZnO/Si-multilayer system tested the sensitivity of the BSE analysis. It was demonstrated that materials with as similar chemical composition as Zn(O_{0.5}S_{0.5}) and Zn(O_{0.7}S_{0.3}) can be distinguished in a BSE image, as suggested by the MC simulations. As second test sample, a PTB7/PC₇₁BM-multilayer system was used as a representative for weakly scattering materials. Based on MC simulations, the most suitable imaging conditions for obtaining the highest contrast between the PTB7 and PC₇₁BM layers were derived. The comparison of the measured and simulated data reveals that the measured PC₇₁BM intensities can be reliably simulated, whereas in the case of the PTB7, significant discrepancies were observed. The most probable origin of the discrepancy is the deviation of the nominal and real chemical composition of PTB7, which may have been modified by electron-beam-induced damage.

Finally, we point out that the screening parameter in the differential Rutherford scattering cross-sections, that are used in the MC simulations, strongly influence the simulated BSE intensities. For quantification of experiment BSE intensities, the most suitable screening parameter must be determined for the materials of interest.

ACKNOWLEDGEMENTS

We thank Dr. Wolfram Witte (ZSW, Zentrum für Sonnenenergie- und Wasserstoffforschung, Stuttgart/Germany) for providing the ZnS/Zn(O_xS_{1-x})/ZnO/Si-multilayer sample. The PTB7/PC₇₁BM-multilayer system was prepared by Dr. Yonghe Li (Laboratory for Electron Microscopy, KIT). We also thank Prof. Dr. Christian Kübel (Institute of Nanotechnology, KIT) for helpful comments.

Open access funding enabled and organized by Projekt DEAL.

ORCID

Martin Čalkovský  <https://orcid.org/0000-0003-2500-9127>

REFERENCES

1. Reimer, L. (1998). *Scanning electron microscopy: Physics of image formation and microanalysis* (second edn.). Berlin, London: Springer.

2. Cazaux, J. (2012). Electron back-scattering coefficient below 5 keV: Analytical expressions and surface-barrier effects. *Journal of Applied Physics*, *112*, 084905.
3. Joy, D. C. (1995). *Monte Carlo modeling for electron microscopy and microanalysis*. Oxford University Press.
4. Joy, D. C. (1991). An introduction to Monte Carlo simulations. *Scanning Microscopy*, *5*, 329–337.
5. Guanira, K., Valente, T. M., Rios, C. A., Castellanos, O. M., Salazar, L., Lattanzi, D., & Jaime, P. (2020). Methodological approach for mineralogical characterization of tailings from a Cu(Au, Ag) Skarn type deposit using QEMSCAN (quantitative evaluation of minerals by scanning electron microscopy). *Journal of Geochemical Exploration*, *209*, 106439.
6. Kim, H., Negishi, T., Kudo, M., Takei, H., & Yasuda, K. (2010). Quantitative backscattered electron imaging of field emission scanning electron microscopy for discrimination of nano-scale elements with nm-order spatial resolution. *Journal of Electron Microscopy*, *59*, 379–385.
7. Roschger, P., Plenk, H., Jr., Klaushofer, K., & Exchberger, J. (1995). A new scanning electron microscopy approach to the quantification of bone mineral distribution: Backscattered electron image grey-levels correlated to calcium K α -line intensities. *Scanning Microscopy*, *9*, 75–88.
8. Garitagoitia Cid, A., Rosenkranz, R., Löffler, M., Clausner, A., Standke, Y., & Zschech, E. (2018). Quantitative analysis of backscattered electron (BSE) contrast using low voltage scanning electron microscopy (LVSEM) and its application to Al_{0.22}Ga_{0.78}N/GaN layers. *Ultramicroscopy*, *195*, 47–52.
9. Müller, E., & Gerthsen, D. (2017). Composition quantification of electron-transparent samples by backscattered electron imaging in scanning electron microscopy. *Ultramicroscopy*, *173*, 71–75.
10. Dapor, M., Bazzanella, N., Toniutti, L., Miotello, A., Crivellari, M., & Gialanella, S. (2013). Backscattered electrons from gold surface films deposited on silicon substrates: A joint experimental and computational investigation to add new potentiality to electron microscopy. *Surface and Interface Analysis*, *45*, 677–681.
11. Haimovich, J., Leibold, K., & Staudt, G. (1996). Estimating and measuring thickness of thin layers by Monte Carlo simulation and backscattered electron image analysis. *The Journal of Technology Transfer*, *5*, 65–78.
12. Niedrig, H. (1977). Film-thickness determination in electron microscopy: The electron backscattering method. *Optica Acta*, *24*, 679–691.
13. Kowoll, T., Müller, E., Fritsch-Decker, S., Hettler, S., Störmer, H., Weiss, C., & Gerthsen, D. (2017). Contrast of backscattered electron SEM images of nanoparticles on substrates with complex structure. *Scanning*, *2017*, 4907457.
14. Aoyama, T., Nagoshi, M., & Sato, K. (2015). Quantitative analysis of angle-selective backscattering electron image of iron oxide and steel. *Microscopy*, *64*, 319–325.
15. Sato, K., Sueyoshi, H., & Yamada, K. (2015). Characterization of complex phase steel using backscattering electron images with controlled collection angles. *Microscopy*, *64*, 297–304.
16. Wan, Q., Plenderleith, R. A., Dapor, M., Rimmer, S., Claeysens, F., & Rodenburg, C. (2015). Separating topographical and chemical analysis of nano-structure of polymer composite in low voltage SEM. *Journal of Physics: Conference Series*, *644*, 012018.
17. Assa'd, A. M. D. (2018). Monte Carlo calculation of the backscattered coefficient of thin films of low on high atomic number materials and the reverse as a function of the incident electron energy and film thickness. *Applied Physics A*, *124*, 699–675.
18. Hannachi, M., Rouabah, Z., Champion, C., & Bouarissa, N. (2014). Electron backscattering from solid targets: Elastic scattering calculations. *Journal of Electron Spectroscopy and Related Phenomena*, *195*, 155–159.
19. Sánchez, E., Torres Deluigi, M., & Castellano, G. (2012). Mean atomic number quantitative assessment in backscattered electron imaging. *Microscopy and Microanalysis*, *18*, 1355–1361.
20. Croccolo, F., & Riccardi, C. (2008). Passive mirror imaging through a solid-state back-scattered electron detector. *Microscopy Today*, *16*, 40–43.
21. Nanver, L. K., Scholtes, T. L. M., Šakić, A., Kooijman, C. S., & van Veen, G. N. A. Radiation detector. US patent 8,450,820 B2, issued May 28, 2013.
22. Ritchie, N. W. M. (2005). A new Monte Carlo application for complex sample geometries. *Surface and Interface Analysis*, *37*, 1006–1011.
23. Joy, D. C., & Luo, S. (1989). An empirical stopping power relationship for low-energy electrons. *Scanning*, *11*, 176–180.
24. Čalkovský, M., Müller, E., Hugenschmidt, M., & Gerthsen, D. (2019). Differential electron scattering cross-sections at low electron energies: The influence of screening parameter. *Ultramicroscopy*, *207*, 112843.
25. Czyżewski, Z., MacCallum, D. O. N., Romig, A., & Joy, D. C. (1990). Calculations of Mott scattering cross section. *Journal of Applied Physics*, *68*, 3066–3072.
26. Gutierrez-Urrutia, I. (2019). Quantitative analysis of electron channeling contrast of dislocations. *Ultramicroscopy*, *2006*, 112836.
27. Jin, X., Schneider, R., Hariskos, D., Bauer, A., Witte, W., Powalla, M., & Gerthsen, D. (2021). Improvement of quantitative STEM/EDXS analyses for chemical analysis of Cu(In,Ga)Se₂ solar cells with Zn(O,S) buffer layers. *Microscopy and Microanalysis*, *27*((S1)), 2060–2063. <https://doi.org/10.1017/S1431927621007467>
28. Haynes, M. W.: (2011). *CRC handbook of chemistry and physics* (92nd edn.). CRC Press.
29. Lide, D. R. (1998). *CRC handbook of chemistry and physics* (79th edn.). Boca Raton, FL: CRC Press.
30. Kyriakou, I., Emfietzoglou, D., Nojeh, A., & Moscovitch, M. (2013). Monte Carlo study of electron-beam penetration and backscattering in multi-walled carbon nanotube materials: The effect of different scattering models. *Journal of Applied Physics*, *113*, 084303.
31. Kurniawan, O., & Ong, V. K. S. (2007). Investigation of range-energy relationships for low-energy electron beams in silicon and gallium nitride. *Scanning*, *29*, 280–286.
32. Goldstein, J. I., Costley, J. L., Lorimer, G. W., & Reed, S. J. B. (1977). Quantitative X-ray analysis in the electron microscope. *Scanning Electron Microscope*, *1*, 315–324.
33. Li, Y., Müller, E., Sprau, C., Colsmann, A., & Gerthsen, D. (2020). Imaging of polymer:Fullerene bulk-heterojunctions in a scanning electron microscope: Methodology aspects and nanomorphology by correlative SEM and STEM. *Advanced Structural and Chemical Imaging*, *6*, 1–12.

34. Rubanov, S., & Munroe, P. R. (2004). FIB-induced damage in silicon. *Journal of Microscopy*, *214*, 213–221.
35. Roehling, J. D., Baran, D., Sit, J., Kassar, T., Ameri, T., Unruh, T., Brabec, C. J., & Moule, A. J. (2016). Nanoscale morphology of PTB7 based organic photovoltaics as a function of fullerene size. *Science Reports*, *6*, 30915.
36. Leijten, Z. J. W. A., Keizer, A. D. A., de With, G., & Friedrich, H. (2017). Quantitative analysis of electron beam damage in organic thin films. *Journal of Physical Chemistry C*, *121*, 10552–10561.
37. Dyck, O., Hu, S., Das, S., Keum, J., Xiao, K., Khomami, B., & Duscher, G. (2015). Quantitative phase fraction detection in organic photovoltaic materials through EELS imaging. *Polymers*, *7*, 2446–2460.
38. Karbovnyk, I., Olenych, I., Aksimentyeva, O., Klym, H., Dzdzelyuk, O., Olenych, Y., & Hrushetska, O. (2016). Effect of radiation on the electrical properties of PEDOT-based nanocomposites. *Nanoscale Research Letters*, *11*, 84.
39. Lenz, A., Kariis, H., Pohl, A., Persson, P., & Ojamäe, L. (2011). The electronic structure and reflectivity of PEDOT:PSS from density functional theory. *Chemical Physics*, *384*, 44–51.
40. Mateker, W. R., Heumueller, T., Cheacharoen, R., Sachs-Quintana, I. T., McGehee, M. D., Warnan, J., Beaujuge, P. M., Liu, X., & Bazan, G. C. (2015). Molecular packing and arrangement govern the photo-oxidative stability of organic photovoltaic materials. *Chemistry of Materials*, *27*, 6345–6353.

How to cite this article: Čalkovský, M., Müller, E., & Gerthsen, D. (2022). Quantitative analysis of backscattered-electron contrast in scanning electron microscopy. *Journal of Microscopy*, 1–16. <https://doi.org/10.1111/jmi.13148>